ADVANCED ENERGY MATERIALS
www.advenergymat.de

Triple Regulation of Water Molecules Behavior to Realize High Stability and Broad Temperature Tolerance in Aqueous Zinc Metal Batteries via a Novel Cost-Effective Eutectic Electrolyte

*Wensong Lv, Yi Tan, Chengyue Guo, Xin He, Lingxing Zeng, Jinliang Zhu, Le Yang, Zhengjun Chen, Xucai Yin, Jing Xu, and Huibing He**

The high activity of water in aqueous electrolyte causes drastic side reactions on the Zn anodes, severely limiting the electrochemical performance of aqueous zinc metal batteries (AZMBs) under extreme conditions. Herein, levulinic acid is developed as the hydrated deep eutectic solvent (DES), to build a novel non-flammable and cost-effective $ZnSO_4$-based eutectic electrolyte with triple regulation of water molecules behavior, enabling highly stable AZMBs over a wide temperature. In situ experiments, molecular dynamics simulations, and spectroscopy analysis jointly reveal that the DES is capable of comprehensively lowering the water activity by simultaneously controlling the behavior of the free, solvated, and interfacial water molecules within the eutectic electrolyte system. Consequently, the Zn anodes exhibit ultralong cycling stability (4500 h at 1 mA cm^{-2}/1 mA h cm^{-2}), decent Coulombic efficiency of 99.39%, and excellent temperature tolerance (−20–50 °C). Notably, the designed 2.0 Ah Zn//VOX pouch cell exhibits a recorded actual energy density of 37.46 Wh Kg^{-1} and 95.38 Wh L^{-1} at the whole cell level, with a remarkable capacity retention of 81.01% after 150 cycles, demonstrating the potential for scale-up into real AZMBs. This work provides an in-depth understanding of the correlation between the water molecule behavior and electrochemical properties of AZMBs.

1. Introduction

The development of low-cost, environmentally friendly, and safe large-scale energy storage technologies is particularly important for the popularization of green renewable energy.[1] Due to the superior capacity of Zn anode (820 mAh g^{-1} and 5855 cm^{-3}), moderate operating potential (−0.76 V vs SHE), inherent safety, and particularly the adoption of water-based electrolytes, aqueous Zn metal batteries (AZMBs) have emerged as a promising candidate for grid-scale energy storage, which has attracted more and more attention in recent years.[2] However, the water plays a double-edged sword role in manipulating the AZMBs performance. Just as an old saying goes, water can carry a boat but also capsize it. On the one hand, the water-based electrolytes with high ionic conductivity enable superior electrochemical performance in AZMBs. On the other hand, the large amount of free water with strong hydrogen bonds, the abundant bound water in the Zn ions solvation structure, and the rampant absorbed water on the Zn electrode interface collectively contribute to the high activity of water molecule, which also triggers the persistent and deep-rooted issues, such as the detrimental Zn dendrites, spontaneous corrosion and by-product aggregation on the Zn electrodes (**Figure 1**a,c), posing a significant threat to the further development of AZMBs.[3] Therefore, reducing the water activity in the aqueous electrolyte system by manipulating the water molecules behavior is the key to stabilizing the Zn anode interface for sustainable and reversible AZMBs.

Up to now, numerous efforts for regulating the behavior of water molecules have been devoted to modulating the interface chemistry in AZMBs, including electrolyte design, anode surface modification, and separator development.[4] Among these strategies, the straightforward and cost-effective electrolyte engineering, which saturates all the components within the cell, has proven to be a highly efficient and practical method for inducing reversible and stable Zn stripping/plating performance.[5]

W. Lv, Y. Tan, C. Guo, J. Zhu, L. Yang, Z. Chen, X. Yin, J. Xu, H. He
School of Chemistry and Chemical Engineering
Guangxi Key Laboratory of Petrochemical Resource Processing and Process Intensification Technology
Guangxi Key Laboratory of Electrochemical Energy Materials
Guangxi University
Nanning 530004, China
E-mail: huibinghe@gxu.edu.cn

X. He
State Key Laboratory of Chem/Bio-Sensing and Chemometrics
College of Chemistry and Chemical Engineering
Hunan University
Changsha 410082, China

L. Zeng
Engineering Research Center of Polymer Green Recycling of Ministry of Education, College of Environmental and Resources
Fujian Normal University
Fuzhou, Fujian 350007, China

The ORCID identification number(s) for the author(s) of this article can be found under https://doi.org/10.1002/aenm.202403689

DOI: 10.1002/aenm.202403689

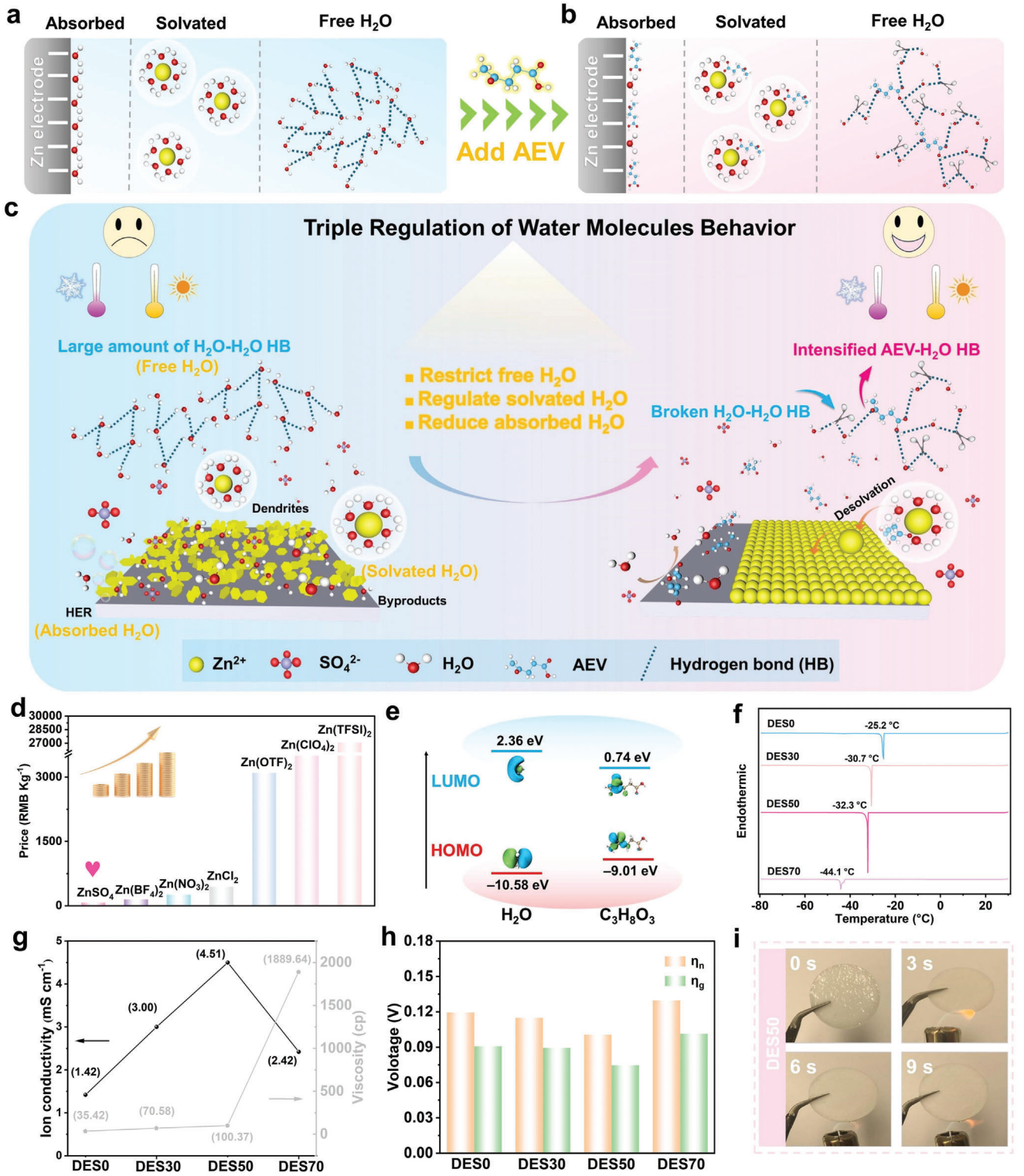

Figure 1. a, b) Schematic illustration of the different behavior characteristics of water molecules in aqueous electrolytes with or without the addition of AEV. c) The effect of triple regulation of water molecules behavior on the electrolyte environment and Zn electrode interface evolution. d) Price of the zinc salts based on the Sigma price list. e) LUMO and HOMO energy values of H_2O, $C_5H_8O_3$ molecules. The corresponding molecular structures and geometry structures are shown in the insets. f) DSC curves of the DES-X electrolytes. g) The ionic conductivity and viscosity of DES-X electrolytes. h) Comparison of the nucleation overpotential (η_n) and growth overpotential (η_g) of DES0, DES30, DES50, and DES70 electrolyte. i) Photographs of the ignition test of the glass fiber after immersing them into the DES50 solution.

In the conventional aqueous electrolytes, the term "water molecule" can be subdivided into three distinct categories: free water, solvent water, and adsorbed water. In general, the introduction of hydrogen bonding acceptor or donor substances into aqueous electrolytes can effectively inhibit the activity of water molecules and lower the freezing point of aqueous electrolytes, which is achieved by breaking the initial H_2O-H_2O hydrogen bonding networks, coordinating with water molecules and restricting the contact of absorbed water molecules. Based on this theory, the introduction of high-concentration electrolytes can effectively reduce the number of free water molecules and effectively break the original hydrogen bonding network between water molecules. The use of high-concentration electrolytes has been demonstrated to effectively alleviate the issues on the zinc anode side, which is achieved by the reduced percentage of free H_2O molecules and alteration in the interfacial ion concentration.[6] For example, Fang et al. developed a high-concentration (30 M) $ZnCl_2$ "water-in-salt" electrolyte,[7] driving the solvation structure of Zn^{2+} shifted from $[Zn(H_2O)_6]^{2+}$ to $[ZnCl_4]^{2+}$ and $[ZnCl_4(H_2O)_2]^{2+}$ when the concentration rises from 5 to 30, resulting in the weakened hydrogen evolution and widened electrochemical window from 1.6 to 2.3 V.[8] Unfortunately, highly concentrated salts are usually expensive and harmful to the environment. Besides, the high viscosity and poor ionic conductivity of the high-concentration solution largely restrict the ion transportation kinetics and further degrade the battery performance.[9] In addition, by adding organic co-solvent to the aqueous solution, the hybrid aqueous electrolyte can offer extremely low freezing points. Most organic functional groups can act as hydrogen bonding acceptors and/or donors, forming strong coordination interactions with water, which allows hybrid aqueous electrolytes to regulate the coordination behavior of bound water in the Zn^{2+} solvation sheath. Despite their low viscosity, organic solvents often present a low boiling or flash point, posing a potential fire hazard. To date, the exploration of novel electrolyte designs combining low concentrate, economic salts, low viscosity, non-flammability and minimal water activity for a wide-temperature operating range, represents a highly urgent and challenging endeavor.

Deep eutectic solvents (DES) are unique types of solvents consisting of two or more components mixture that interact with each other through hydrogen bonding.[10] The DES are characterized by solidifying at significantly lower temperatures than their individual constituent,[11] owing to the remodeled solvation structure from conventional water or organic solvents. Compared to the aqueous solvents, DES feature stable and organized solvation structure,[12] which aids in coordinating with Zn^{2+}, and forms a new HB network with H_2O, thereby diminishing active H_2O molecules within the solvation layer and extending the electrochemical window of the electrolytes. As a result, the Zn deposition becomes more uniform and less side reactions occur on the electrode surface. Ciucci et al. developed a new type of DES containing sulfolane (SL) and $Zn(ClO_4)_2{\cdot}6H_2O$.[13] Such unique water-in-DES structure reduced the water activity, with expanded electrochemical window and enhanced Zn^{2+} deposition quality. Although DESs are economically feasible, nonflammable, and stable, they are characterized by a high binding energy that brings about substantial electrolyte viscosity, which can slow down the ion transport and increase the battery polarization. To address this challenge, researchers are exploring small molecule cosolvents with strong polarity, low viscosity, and a large dielectric constant,[11b] which can tightly control the amount of water molecules to maintain the optimal solvated structure and ionic conductivity.

Here, due to 2M $ZnSO_4$ that has been used in the eutectic electrolyte,[14] and levulinic acid ($C_5H_8O_3$) with its low cost, moderate Lewis alkalinity, and excellent electrochemical/physical properties,[15] we have developed a novel DES-based aqueous electrolyte consisting of x vol % levulinic acid and (1-x) vol % water as the co-solvent, and 2M $ZnSO_4$ as the solute (denoted as DES-X). In comparison, the electrolyte in the control group involves water as the sole solvent (DES-0). As shown in Figure 1b,c the preferential adsorption of AEV molecule reduces the presence of adsorbed water on the Zn surface, resulting in suppressing drastic side-reactions.[16] Besides, the eutectic electrolyte could simultaneously regulate dipolar-molecule (AEV-H_2O) and dipolar-ion (AEV-Zn^{2+}) interactions, thus to reshape the hydrogen-bond (HB) network and Zn^{2+} solvation sheath. Subsequently, large amount of the free H_2O is captured by AEV-H_2O HB network, thus to broaden the battery operating temperature range. Meanwhile, the solvated H_2O is replaced by AEV molecules to enter into the Zn^{2+} solvation sheath to diminish the active water number upon Zn plating process. As a result, the zinc dendrite, HER, and corrosion are largely inhibited. The fabricated Zn|DES50|Zn symmetrical cells produce outstanding cyclic performance (over 1800 h at 5 mA cm^{-2}, 650 h even at a high depth of discharge (DOD) of 80%, and wide operating temperature range of −20~50 °C). Moreover, the Zn//VOX full cells demonstrate excellent cycling stability at both high (50 °C) and low temperatures (−20 °C). Encouragingly, the designed 2.0 Ah Zn//VOX pouch cell harvests an actual energy density of 37.46 Wh Kg_{cell}^{-1} and 95.38 Wh L_{cell}^{-1}, with a considerable capacity retention of 81.01% after 150 cycles. These findings offer new insights into the development of low-cost and effective eutectic electrolytes for practical AZMBs.

2. Results and Discussion

The high cost of the Zn salts in the DES electrolyte has been a significant obstacle to the advancement of AZMBs. In order to reduce the cost of electrolytes, the cheapest zinc sulphate salts are selected (Figure 1d). To demonstrate the electrochemical stability of different solvent molecules of AEV and H_2O, we calculated their lowest unoccupied molecular orbital (LUMO) and highest occupied molecular orbital (HOMO) energies. AEV exhibits both a higher LUMO (0.74 vs. 0.55 eV) and lower HOMO (−9.01 vs. −8.81 eV) value compared to H_2O, suggesting that AEV molecule is more resistant to accept/lose electrons from the Zn anode than free H_2O (Figure 1e), which may be beneficial for broadening the electrochemical stability window of the electrolyte.[17] Most importantly, an AEV molecule contains two dipoles (—COOH and —C═O) that can both act as the hydrogen bond acceptor, which is expected to effectively disrupt the original HB network by forming enhanced hydrogen bonding interactions with water (water acts as a hydrogen bond donor). Thus, aqueous hybrid electrolytes with AEV as co-solvent can attain a low freezing point (Figure S1, Supporting Information).[18]

Considering the adverse effect of the high viscosity and low ionic conductivity of eutectic electrolytes at room temperature, we prepare a series of aqueous DES electrolytes with varied volume ratios of water to AEV. All the DESs are homogeneous and colorless liquid at room temperature. As shown in Figure 1f, the freezing point of DES-X decreases gradually as the proportion of AEV increases due to the ability of DES electrolyte to intensify AEV-H_2O HB getting stronger. Notably, the molar ratio of these two substances significantly influences the hydrogen bond network within the liquid, as demonstrated by the temperature difference in the freezing point. Specifically, the optimized AEV ratio was determined by the physical and electrochemical properties. Among all the DES-X electrolytes, the DES50 has the highest ion conductivity (4.51 mS cm^{-1}) with moderate viscosity (100.37 cp) (Figure 1g; Figure S2, Supporting Information). Meanwhile, the introduction of organic AEV co-solvent also affects the zinc nucleation overpotential (η_n) and growth overpotential (η_g) on the Zn electrode. Both the η_n and η_g gradually decrease when the AEV ratio increases from DES0 to DES50 (Figure 1h; Figure S3, Supporting Information), which is beneficial for the uniform plating/stripping process.[8] However, limited by the low ionic conductivity and high viscosity, the η_n and η_g in DES70 turns to increase. Therefore, the DES50 is selected for the optimized eutectic electrolyte in the following study. In addition, the Fourier transform infrared (FT-IR) spectra show that the stretching vibration of carbonyl group in DES50 presents red shift compared with the pure AEV (Figure S4, Supporting Information), indicating the coordination of Zn^{2+} with oxygen in AEV and the successful construction of eutectic electrolyte system. As AEV is a flammable organic solvent, it is necessary to conduct ignition testing on the DES electrolytes (Figure 1i). The DES50-soaked glass fiber separators did not catch fire after 9 s ignition tests, which identified the non-flammable nature and high security of the AEV-containing eutectic electrolytes.

The mechanism of dendrite growth and side reaction inhibition by DES50 was systematically investigated through theoretical calculations and experimental characterizations. Within the eutectic system, hydrogen bond donors and acceptors are necessary to create a stable H-bond network. The electrostatic potential calculations (ESP) map of an AEV molecule reveals that C═O group is much attractive to hydrogen atoms because of its prime negative charge distribution, providing more strong nucleophilic sites for cationic and hydrogen bond donors (**Figure 2a**).[16,19] The interaction of hydrogen bonds and solvation structures in various electrolytes was explained. The O−H stretching modes of water molecules (bending vibration 1600–1700 cm^{-1} and stretching vibration 3000–3500 cm^{-1}) were detected in the FTIR spectra,[20] showing a noticeable shift to lower wavenumbers with increased AEV concentration (DES0: 3613.02 cm^{-1}, DES50: 3611.02 cm^{-1}, and DES70: 3602.93 cm^{-1}) (Figure 2b). The result illustrates that the carbonyl group of the AEV molecule tends to coordinate with Zn^{2+}, replacing the H_2O molecule. Generally, the decrease of free water molecules suppresses the formation of $[Zn(H_2O)_6]^{2+}$ and slows down the water decomposition. Additionally, local Raman spectroscopy of the electrolytes (O−H stretching vibration at 3200–3500 cm^{-1}) further verified the solvation behavior of the AEV co-solvent in the DES solution. As the AEV concentration increases, the peaks of the O−H stretching band in Raman spectra (Figure S5, Supporting Information) shifted to higher positions, indicating that AEV co-solvent has effectively altered the coordination environment around Zn^{2+} and reduced the number of active H_2O molecules (free water molecules). To further analyze the H-bond states in different electrolytes, their percentages were calculated based on the areas of the three fitted peaks (Figure S6a,b, Supporting Information). As presented, the ratios of strong H-bond are gradually increased while the weak H-bond decreased with the increased concentration of AEV, suggesting the progressive devastation of the H-bond structure by increasing the AEV content. Furthermore, the decreased availability of free water was also supported by the nuclear magnetic resonance (NMR) spectroscopy (Figure 2c). The ^1H peak of DES0 was centered at 4.7174 ppm, which gradually shifted to a lower field (a higher chemical shift) at 4.7207 and 4.7246 ppm with 50 and 70 vol% of DES, respectively. The spectroscopic results suggest the strong coordination between Zn^{2+} and AEV, which results in the decreased electron cloud density around the free H_2O with a de-shielding effect.[21]

Molecular dynamics (MD) simulations coupled with density functional theory (DFT) calculations were employed to investigate the solvation structure and hydrogen bond state of DES0 and DES50 (Figure 2d,g). As depicted in Figure 2h,e, the coordination number (CN) for Zn^{2+}-H_2O in the DES50 (CN = 5) is lower than that in DES0 (CN = 6), implying that the AEV successfully enters the first solvation sheath of Zn^{2+}, with approximately one AEV molecule with an average distance of 2.10 Å. Meanwhile, the state of hydrogen bond structure in different electrolytes is analyzed (Figure 2f,i). The addition of AEV destroys the weak hydrogen bond structure between H_2O molecules, reducing the average hydrogen bond ratio from 78.20% to 45.4%. Instead, a new kind of stable hydrogen bond structure with intensity of 14.1% is created between AEV and H_2O. The MD simulation results align with the DFT calculation, which shows the binding energy of AEV-H_2O (16.260 kcal mol^{-1}) is higher than that of H_2O-H_2O (3.552 kcal mol^{-1}). Due to the introduction of AEV, the H_2O of Zn^{2+} solvation shell and the content of weak hydrogen bond of $H_2O\cdots H_2O$ are significantly reduced, which tremendously inhibits the corrosion of the Zn anode. The Tafel plots further support this conclusion, demonstrating that the addition of AEV leads to the decreased corrosion current density (I_{corr}) and more positive corrosion potential (Figure S7 Supporting Information). Within the eutectic electrolyte system, the binding energy of AEV to Zn^{2+} is greater compared to those of AEV-H_2O and H_2O-Zn^{2+} (Figure 2j). The larger binding energy also leads the lower formation energy of the solvated molecules of $[(Zn(H_2O)_5AEV]^{2+}$, as shown in Figure 2k.[22] In addition, the electrochemical stability window (ESW) of electrolyte was evaluated using electrochemical linear sweep voltammetry (LSV). As the altered hydrogen bonding structure of DES50, the formation of a stronger hydrogen bond structure between AEV and H_2O molecules inhibits the transfer of protons/hydroxides and the separation of ionic products in the Volmer step.[21a] With the increase of AEV content, the ESW of electrolyte is expanded from 1.31 to 2.52 V and hydrogen evolution overpotential increases from 0.38 to −0.19 V (Figure S8, Supporting Information).[23] Meanwhile, DES50 owns the highest Zn^{2+} transference number (t_{Zn}^{2+} = 0.68, Figure 2l; Figure S9 Supporting Information) among the DES-X electrolyte system.

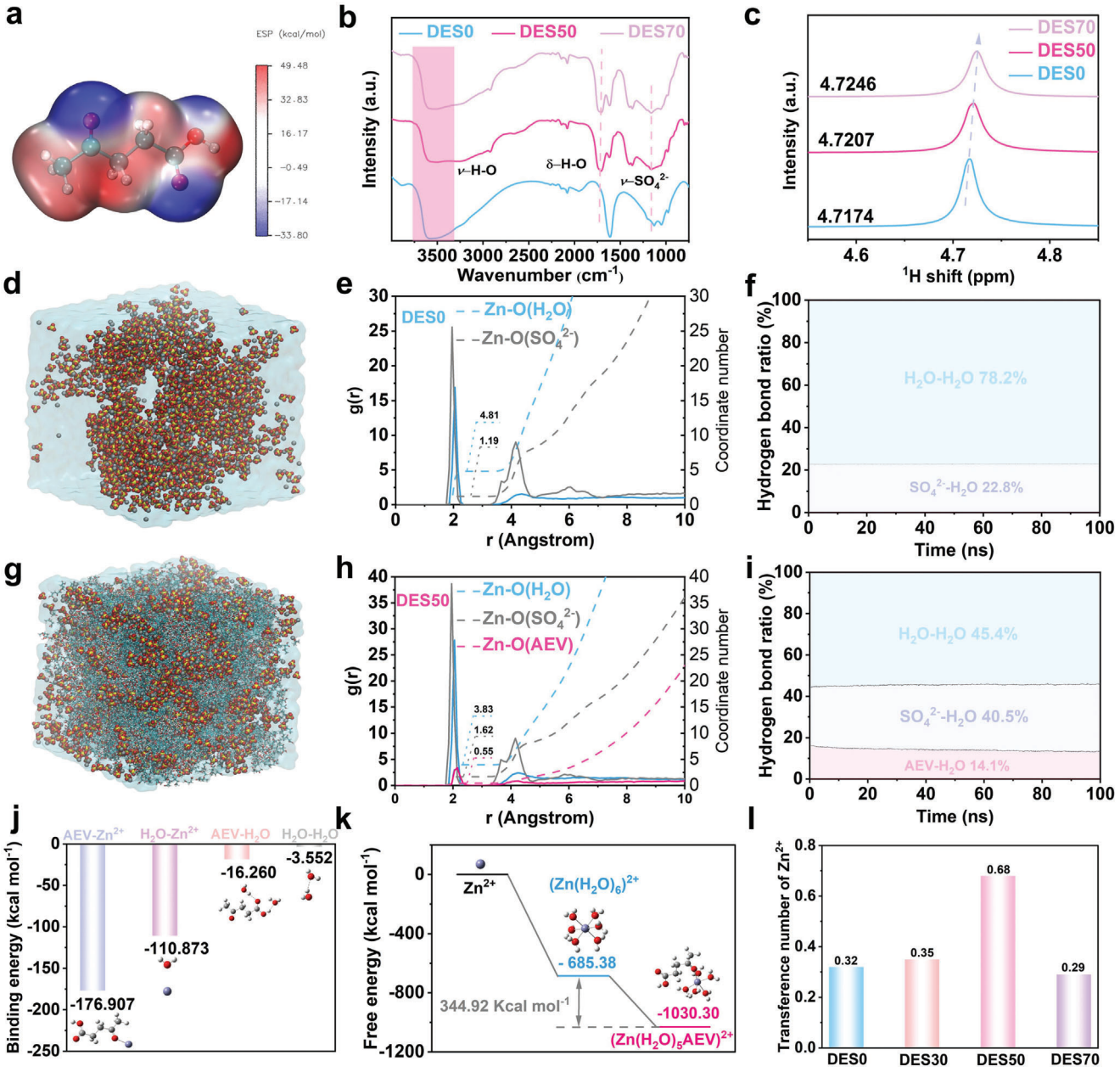

Figure 2. a) The electrostatic potential map of an AEV molecule. b) FTIR spectra of O-H bending vibration peaks between 1500–1800 cm^{-1} and 3000–3600 cm^{-1}. c) ^{1}H NMR spectra of different solutions. d,g) Molecular dynamics (MD) calculation simulation diagrams for $ZnSO_4$ and $ZnSO_4$ -AEV. e,h) Simulated radial distribution functions (RDFs) and coordination number (CN) of Zn^{2+}in DES0 and DES50 electrolyte. f,i) different types of hydrogen bonds ratio collected from the MD simulation of DES0 and DES50. j) Binding energies for Zn^{2+} with AEV, Zn^{2+} with H_2O, AEV with H_2O, and H_2O with H_2O. k) Free energy changes the solvation structure of from $[(Zn(H_2O)_6]^{2+}$ to $[(Zn\text{-}(H_2O)_5AEV]^{2+}$. l) The Zn^{2+} transference number of DES-X.

The optical images revealed that the zinc anode soaked in DES50 remained clean over seven days. In contrast, the zinc anode submerged in DES0 was severely corroded, resulting in a rough and uneven surface (Figure S10, Supporting Information). The enhanced anti-corrosion performance of Zn anode in DES50 electrolyte could be ascribed from the absorption behavior of AEV molecules on the Zn anode, which was investigated by using energy dispersive X-ray spectroscopy (EDS) (**Figure 3**a,b; Figure S11, Supporting Information). The uniform distribution of C, O, S and Zn elements suggests that AEV molecules fully cover the Zn metal surface, thus protecting the Zn anode from the water-induced erosion. XRD analysis was performed to analyze the crystal phase composition of Zn foil after immersion in DES0 and DES50 electrolytes (Figure 3c). The characteristic peaks of the $Zn_4SO_4(OH)_6{\cdot}xH_2O$ (ZSH) by-product appear in the XRD pattern of the Zn foil after immersion in DES0, but no obvious ZSH-related peaks were observed in the DES50. Generally, in the pure $ZnSO_4$ solution (DES0), the corrosion reaction

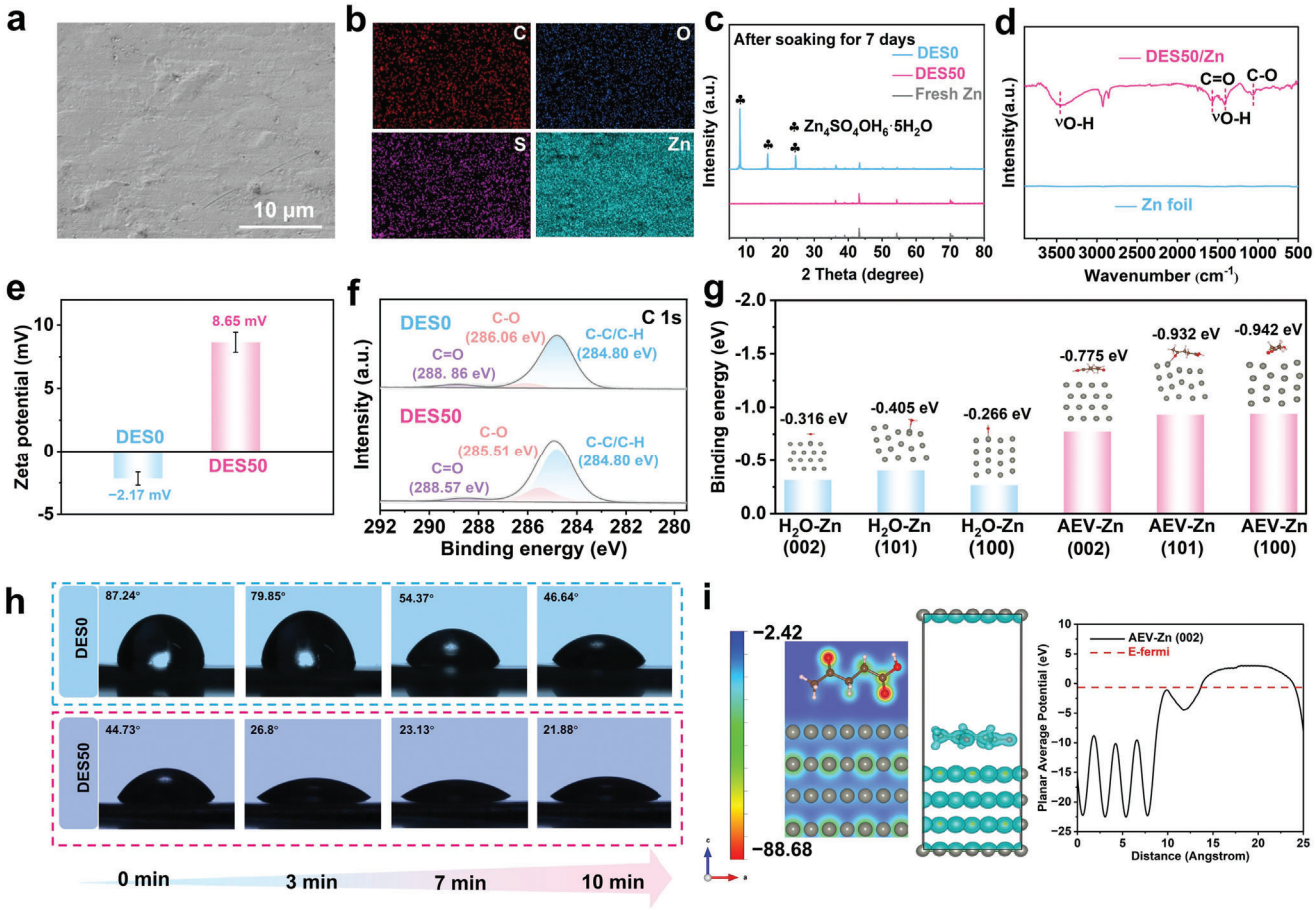

Figure 3. a) SEM image and the corresponding EDS mappings of b) C, O, and S, Zn element on the Zn metal foil after immersing into the DES50 solution. c) XRD patterns of the Zn anode after immersing into the different electrolytes for 7 days. d) ATR-FTIR spectrum of the pristine Zn foil and the Zn foil in DES50. e) Zeta potentials of Zn anodes in DES0/DES50 for one day. f) XPS spectra of C 1s for the Zn foil after immersion in DES0/DES50. g) Comparison of the absorption energy of H_2O and AEV molecules on the Zn (002), Zn (101), and Zn (100) plane with the optimized recumbent adsorption mode. h) Change in contact angle of DES0 and DES50 over time. i) Side view of ELF results for Zn (002) slab with AEV and the planar average potential from Zn (002) surface to the interface adsorbing AEV.

generates the by-products ZSH (PDF#39-0688) on the Zn foil, as shown in the following Equation (1–3):[24]

$$Zn \rightarrow Zn^{2+} + 2e^- \quad (1)$$

$$2H_2O + 2e^- \rightarrow H_2 + 2OH^- \quad (2)$$

$$4Zn^{2+} + 6OH^- + SO_4^{2-} + xH_2O \rightarrow Zn_4SO_4(OH)_6 \cdot xH_2O \quad (3)$$

As shown in the SEM images and EDS spectrum (Figure S12, Supporting Information), abundant irregular hexagonal ZSH nanosheets randomly grew and distributed on the Zn surface after immersion in the DES0 electrolyte for 7 days, with the proportion of O and S content reaching 41.21%, confirming the generation of plentiful ZSH by-products. As anticipated, the surface of the zinc foil remained smooth and flat after being immersed in the DES50 electrolyte, with a much lower percentage of S signal detection, suggesting the suppressed ZHS formation. The presence of C and O may be attributed to a portion of AEV that was adsorbed onto the Zn metal, confirming that AEV could be firmly adhered onto the Zn anode.

The surface chemistry evolution after immersion was investigated using Attenuated Total Reflection Fourier Transform Infrared Spectroscopy (ATR-FTIR) spectrum (Figure 3d). The board peak locating at 3445 cm^{-1} is attributed to the O−H asymmetric stretching vibration. Besides, the peak at 1416 cm^{-1} is assigned to the O−H asymmetric bending vibration. The characteristic peaks at 1563, 1059 cm^{-1} can be assigned to the in-plane bending vibration of C═O, and the asymmetric stretching vibration of −C−O of AEV molecule, respectively.[25] The coordination between AEV and Zn^{2+} was also clearly verified by the increased Zeta potential of Zn anode from −2.17 mV (DES0) to 8.65 mV (DES50), (Figure 3e), indicating that the O-rich functional group in AEV can capture Zn^{2+} in the electrolyte through the coordination with Zn^{2+}. The regulated Zn^{2+} coordination environment not only restricts the random diffusion of Zn^{2+}, to induce rearrangement of ion distribution,[26] but also reduces the quantity of coordinated water molecules, thereby suppressing the H_2O-induced side reactions.[27] Moreover, the XPS results further confirmed

the AEV molecules adsorption. As shown in Figure 3f, the C 1s peak can be deconvoluted into three species originating from the —C═O, —C—O and —C—C/C—H bonds, respectively.[28] Due to the AEV molecules have strong polar functional groups (—C═O), the XPS spectrum of Zn foil immersed in DES50 electrolyte shows that the characteristic peak intensity of C═O (288.57 eV) is higher than that of the corresponding peak (C═O) (288.86 eV) immersed in DES0. Additionally, for the Zn foil after immersion in DES50 electrolyte, the distinct signals at 510.10 eV for C═O in the O 1s spectrum are detected, which is attributed to adsorbed AEV molecule (Figure S13, Supporting Information). In contrast, due to the presence of a by-product ($Zn_4SO_4(OH)_6{\cdot}xH_2O$), a characteristic O 1s peak of OH^- (529.68 eV) appears after immersion in the DES0 electrolyte.[29]

DFT calculations were further carried out to excavate the underlying adsorption mechanisms of AEV and H_2O molecules on Zn metal anode. As presented in Figure 3g, AEV delivers significantly more negative adsorption energies than the H_2O molecule, no matter on which crystal planes and surface sites of Zn crystal, confirming the preferential adsorption of AEV on the surface of Zn metal. Specifically, the absorption mode of AEV with different states on the Zn (002), (101), and (100) plane was also investigated to find out the optimized absorption configurations between the Zn anode and AEV molecules (Figure S14, Supporting Information). The AEV placed in a recumbent position exhibits a lower absorption energy compared to that of AEV placed vertically or parallelly on both the Zn (002) and (100) planes. Besides, the vertically placed AEV owns the lowest absorption energy than the recumbent and parallel mode on Zn (101) plane. The DFT calaculations results suggest that AEV is preferentially adsorbed on the Zn anode whether in a recumbent state on the Zn (002) and (100) planes or a parallel state on the Zn (101) plane.[30]

To support the priority adsorption of AEV, the dynamic contact angle was measured to determine the wettability of DESX (X = 0 and 50) on the surface of the Zn substrate. DES0 displays a larger contact angle of 87.24° than DES50 (44.73°). The difference of ≈25° in the contact angle was maintained as evidenced by the contact angle of 46.64° in DES0 and 21.88° in DES50 after 10 min of rest (Figure 3h).[31] Preferentially adsorbed AEV exists in the electric double layer (EDL), which is advantageous for occupying the reactive sites to avoid the hydrogen production and homogenize the zinc electrodeposition. The electron transfer from the Zn metal to the interface is simulated using the electron localization function (ELF). As shown in Figure 3i, a shielding buffer layer is constructed on the (002) of Zn with enriched electrons, which will decrease the deposition rate of the fast-moving cations.[16] The distribution of ELF was confirmed by the decrease in planar average potential for the Zn slab with parallelly adsorbed AEV. Additionally, the shielding buffer layer with different states on the Zn (101) and (100) plane was also measured by ELF, and the planar average potential for the Zn slab also reduced when AEV was adsorbed parallelly (Figures S15 and S16, Supporting Information). Therefore, it is predicted that the preferentially adsorbed AEV molecules could effectively inhibit the dendrite growth to protect the Zn anode by adjusting the localized electronic structure.

Moreover, the electric double-layer capacitance (EDLC) of Zn anodes was also investigated to demonstrate the absorption effect of AEV molecule on the EDL structure. The larger calculated EDLC in the DES50 (67.43 μF cm^{-2}) compared with that of the control sample (31.77 μF cm^{-2}) confirms the thickened EDL by AEV adsorption (Figure S17, Supporting Information).[32] The AEV molecules will replace the absorbed H_2O dipoles to reduce the water content at the EDL layer, thus suppressing the various side reactions. To further show the inhibition of the side reactions enabled by the AEV molecules adsorption, dynamic measurement of Zn//Zn symmetric cells with alternative cycling and resting measurement was carried out under rigorous conditions that repeat the step of cycling and resting at 1 mA cm^{-2}, 1 mAh cm^{-2} (Figure S18, Supporting Information). The DES0 symmetric cells exhibit short-circuit after only two restarts, while the DES50 symmetric cells show extremely long and stable voltage hysteresis for cycling more than 4500 h. The above results strongly confirm the superior performance of AEV molecules adsorption and inhibited water-related side reactions, which are substantially important to guarantee the long-lasting ZIBs in aqueous system.[33]

A classical EDL model is composed of a Helmholtz plane (HP) layer and a diffusion layer. (Figure S19, Supporting Information) illustrates the evolution of the EDL structure before and after the introduction of AEV co-solvent. Water dipoles tends to absorb on the anode surface rather than the hydrated Zn^{2+} ions ($Zn(H_2O)_6^{2+}$) with large dehydrate energy.[34] Therefore, a H_2O-rich interface has been constructed on the surface of Zn in the DES0 electrolyte. And the zinc metal surface acquires a negative charge, which is expected to repel anion molecules primarily to the region outside the outer Helmholtz plane (OHP). However, in the DES50 electrolyte, the preferentially absorbed AEV molecules would replace free H_2O to absorb on the Zn anode surface, reconstructing an H_2O-poor HP layer. Besides, in the diffusion layer of EDL, a large amount of H_2O-H_2O HB is broken, with building of a brand new AEV-H_2O HB network. Throughout the EDL, the activity of a large quantity of free water is significantly reduced, which definitely suppresses the water-induced side reactions.[35]

To assess the impact of DES50-regulated EDL structure on the Zn deposition behavior, **Figure 4a** displays the cyclic voltammetry (CV) curves of the Zn//Cu asymmetric cells tested in different electrolytes. The nucleation overpotential was denoted as the gap between the crossover point B and the point A/A′ where Zn^{2+} ions was first to be reduced.[36] Notably, the Zn nucleation overpotential was smaller in the DES50 electrolyte than that in the DES0 electrolyte, suggesting a higher Zn deposition kinetics and a lower nucleation barrier in the DES50 electrolyte system. Moreover, the Zn//Zn symmetric cell with DES50 electrolyte exhibits larger integrated peak areas compared with the cell with DES0 electrolyte (Figure S20, Supporting Information), demonstrating the improved interfacial activity enabled by the AEV molecules absorption, which leads to a rapid transfer of Zn^{2+} and activates more nucleation sites for Zn^{2+} deposition.[37] The increasing nucleation sites and distinct zinc deposition patterns were also proved through the chronoamperometry (CA) measurement (Figure 4b). In the DES0 electrolyte, the current density of the cell continuously increases, indicating an uncontrolled 2D diffusion of zinc ions. In contrast, the cell in the DES50 electrolyte achieves a steady current density only after initial 50 s, reflecting the constant 3D diffusion of Zn^{2+} after Zn nucleation,[38] which helps mitigate the "tip effect", and finally induces uniform Zn deposition. In addition, the linear sweep voltammetry (LSV) test showed a negative shift in HER onset potential in the DES50

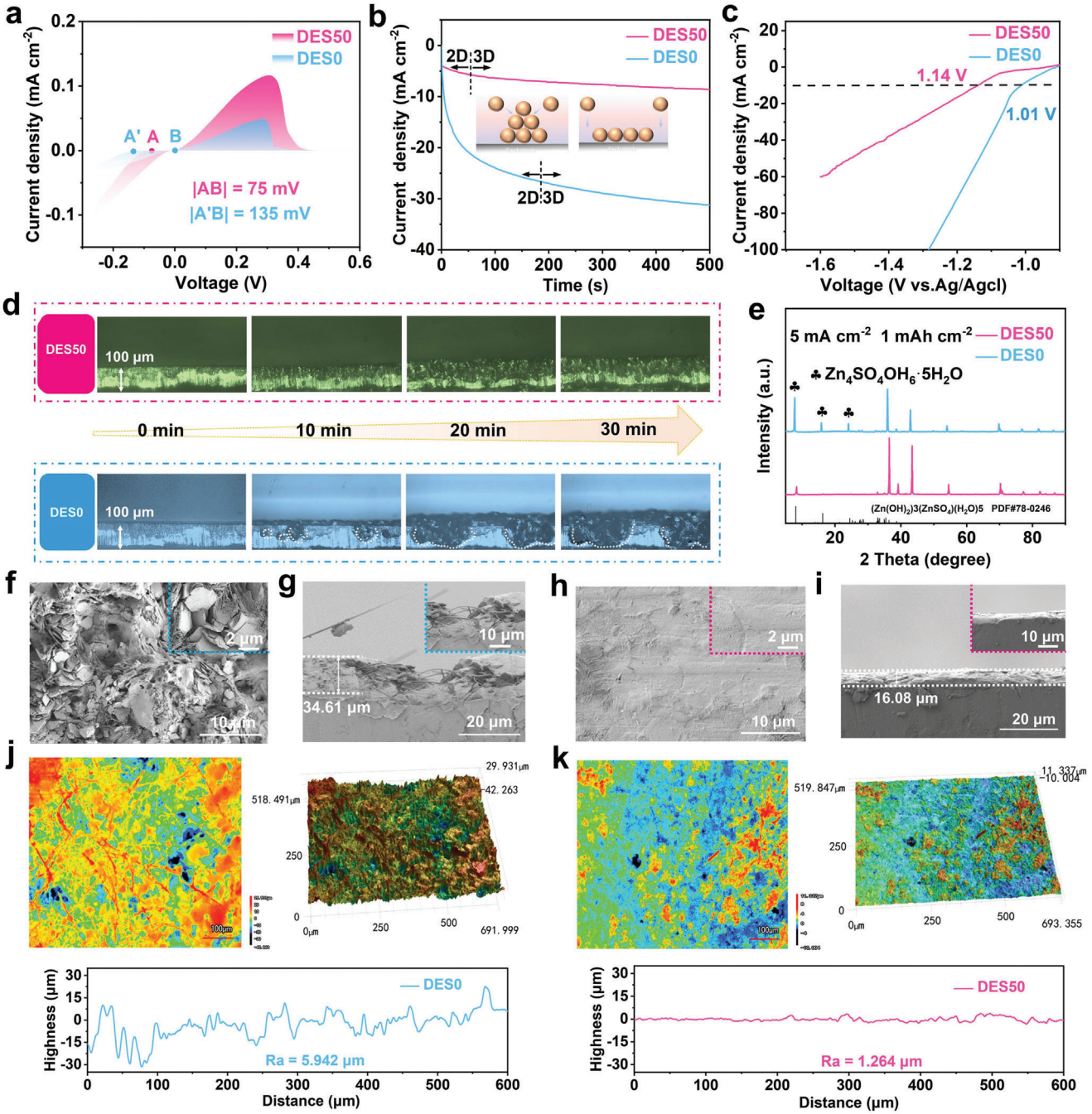

Figure 4. a) Cyclic voltammetry (CV) curves of the Zn//Cu asymmetric cells. b) CA curves at −150 mV overpotential. Insets are the schematic illustrations of the 2D diffusion and 3D diffusion of Zn^{2+}. c) Hydrogen evolution reaction (HER) performance of the Zn anode in the DES0/DES50. d) In situ optical microscope observation of Zn deposition in the DES0/DES50 at 10 mA cm^{-2}. e) XRD patterns of the Zn electrodes after 50 cycles in DES0 and DES50. Top-view and side-view SEM images of the Zn anode cycled in DES0 (f, g) and DES50 (h, i). 3D CLSM images and the corresponding surface roughness curves of Zn anodes cycling in DES0 (j) DES50 (k) after plating.

electrolyte compared with DES0 electrolyte, indicating the better ability of DES50 to suppress hydrogen evolution reaction (Figure 4c). SEM images were captured for the cycled Zn foil in DES0 or DES50 electrolytes (Figure S21a,b, Supporting Information). After 10 cycles in the DES0 electrolyte, a few by-products and Zn dendrites were formed on the surface of the Zn metal. With the increased number of cycles beyond 50, numerous sharp and irregular ZSH particles, as well as Zn dendrites and deposition holes, appeared on the Zn anode. The phenomenon becomes more noticeable after 100 cycles. However, the Zn foil cycled in the DES50 electrolyte remained smooth and flat as the number of cycles increased, with no dendrites or by-products

observed. The results indicate the effective inhibition of Zn dendrite formation and harmful reactions induced by the DES50 electrolyte.

In situ optical microscope was utilized to visually highlight the regulated zinc deposition behavior on the Zn foil electrode. In the DES0 electrolyte, obvious Zn corrosion emerges on the Zn surface after 10 min plating and constantly expands in the later 20 min. As the deposition time prolongs, the zinc deposition layer becomes much thicker on the Zn metal. Furthermore, the deposited layer of Zn appeared to be fluffy in the form of dendrites, which could potentially lead to a poor Coulombic efficiency (CE), battery performance degradation, and further the internal cell short-circuits (Figure 4d). In sharp contrast, during the entire 30-min plating process, the surface of the Zn electrode in the DES50 maintains a dense and uniform deposition morphology, without any dendritic protrusions. Based on the excellent performance of the DES50 electrolyte in inhibiting Zn dendrite formation and detrimental reactions, the Zn//Zn symmetric cell exhibited a cycle life of over 1600 h (1 mA cm^{-2}, 1 mAh cm^{-2}), 350 h (1 mA cm^{-2}, 10 mAh cm^{-2}) and 720 h (5 mA cm^{-2}, 2.5 mAh cm^{-2}), as shown in Figures S22–S24 (Supporting Information), respectively. However, in the DES0 electrolyte, the Zn//Zn symmetric cell failed after cycling of only 80 h (1 mA cm^{-2}, 1 mAh cm^{-2}), 50 h (1 mA cm^{-2}, 10 mAh cm^{-2}) and 40 h (5 mA cm^{-2}, 2.5 mAh cm^{-2}. Crystal phase and surface morphology characterizations for the cycled Zn anodes were implemented to figure out the reasons behind the exceptional Zn stripping/plating performance. Figure 4e shows the XRD patterns of the Zn foil after cycling in DES0/DES50 electrolytes. There is no XRD peaks for ZHS by-products detected on the surface of the Zn anode after 200 cycles at 1 mA cm^{-2} and 1 mAh cm^{-2} in DES50 electrolyte. Similar conclusions can also be drawn from the SEM observations and confocal laser scanning microscopy (CLSM) images. In the DES0 electrolyte, the surface of the cycled Zn electrode was covered with irregular flake-like dendrites and by-products, displaying a highly uneven deposition of Zn (Figure 4f,g). In stark comparison, the Zn electrode in the DES50 electrolyte exhibits a dense and smooth surface without any observed Zn protrusions or dendrites, suggesting the uniform electrochemical Zn plating and stripping during repeated cycles (Figure 4h,i).[39] Conspicuously, the surface of cycled Zn anode in the DES0 electrolyte exhibits an undulating protrusion with a maximum roughness of 29.931 µm (Figure 4j), while a relatively flat and dense surface with a value of only 11.337 µm can be found in the 3D confocal image of the Zn anode operating in the DES50 electrolyte (Figure 4k).

The Zn anodes reversibility was evaluated by measuring the CE of Zn plating and stripping using asymmetric Zn//Cu cells at 0.5 mA cm^{-2} and 0.5 mA h cm^{-2} (**Figure 5**a). The CE of Zn//Cu cell in DES0 decayed quickly after 35 cycles with severe voltage fluctuations, which may be ascribed to the dendrite-induced localized short circuiting during cycling. On the contrary, the cell in DES50 maintained a high average CE of 99.39% for over 300 cycles. Accordingly, the nearly overlapped voltage curves for the selected cycles of the Zn//Cu cell using the DES50 electrolyte also indicates the reversible Zn stripping/plating process with much reduced electrode polarization. (Figure S25, Supporting Information). To further verify the outstanding Zn stripping/plating reversibility, CE at an area capacity of 1 mA h cm^{-2} with a higher current density of 5 mA cm^{-2} was also investigated in Zn//Ti cells (Figure S26, Supporting Information), where the Zn//Ti cell with DES50 also showed higher CE than the controlled DES0. The cycling properties of the Zn//Zn symmetric cells at a high current density of 5 mA cm^{-2} are shown in Figure 5b. The Zn//Zn symmetric cell in the DES0 electrolyte fails after only 50 h of cycling due to the intensive voltage fluctuations, while the cycle time of the Zn//Zn symmetric cell in the DES50 electrolyte is greatly extended to 1800 h by a factor of 36, indicating the stable and reversible Zn plating/stripping performance. To demonstrate the effectiveness of our proposed strategy, we compared the performance of Zn//Zn symmetric cells with other works focusing on electrolyte engineering (Figure 5c; Table S1, Supporting Information). The performance of our battery with DES50 is the state-of-the-art one among the previous works, highlighting the positive role of AEV co-solvent in achieving high cumulative capacity, which is a key index for practical applications. The cycling stability of Zn anodes under high depth of discharge (DOD) is regarded as a reliable indicator for evaluating metal-anode-based battery systems. Surprisingly, the cell assembled with DES50 electrolyte exhibits a deep cycling performance for nearly 650 h at a high DOD of 80% (Figure 5d). In comparison, the cell in the DES0 electrolyte happens a short circuit only after 60 h during the second discharge cycle, indicating its poor deep-cycling capability in the blank $ZnSO_4$ electrolyte. The step-by-step rate performance provides additional evidence for the improved reversibility of the Zn anode under various current densities ranging from 0.5 to 5 mA cm^{-2}, with a fixed capacity of 1 mAh cm^{-2} (Figure 5e). The cell using DES50 electrolyte demonstrates a stable voltage hysteresis throughout the examination time of 120 h. In contrast, the cell with DES0 electrolyte experiences a short-circuit after 39 h when the current density increases to 1 mA cm^{-2}.

In particular, the hydrated eutectic electrolyte exhibits good electrochemical properties under extreme conditions due to the strong hydrogen bonding interactions between the AEV solvent and water molecules, which extend the battery cycling temperature range.[40] Even at a low temperature of −20 °C, the symmetrical Zn//Zn cells with DES50 maintained good stability for 720 h at a current density of 0.25 mA cm^{-2} and an areal capacity of 0.25 mAh cm^{-2} (Figure 5f). However, DES0 electrolyte at −20 °C prevents the cell from operating normally. Likewise, the Zn//Zn cell with DES50 exhibited an extended lifespan of over 200 h at 50 °C under the same current density and area capacity (Figure 5g). In contrast, the cells containing DES0 suffered a sudden short circuit after only 40 h of plating/stripping maybe due to the thermo-driven side reactions and severe dendrite growth at high temperatures. These findings demonstrate the exceptional stability of the Zn anode facilitated by the DES50 eutectic electrolyte whether the battery operates under normal or extreme conditions, showing promising prospects in the pursuit of all-climate aqueous AZMBs.

To assess the feasibility of the DES eutectic electrolyte in practical battery applications, the commercial vanadium oxide xerogel (VOX) powder was synthesized and used as the cathode material to assemble the "rocking-chair" Zn//VOX full cells (**Figure 6**a; Figure S27, Supporting Information).[41] In the rechargeable Zn//VOX battery system, DES50 or DES0, glass fiber, and Zn foil are used as electrolyte, separator, and anode,

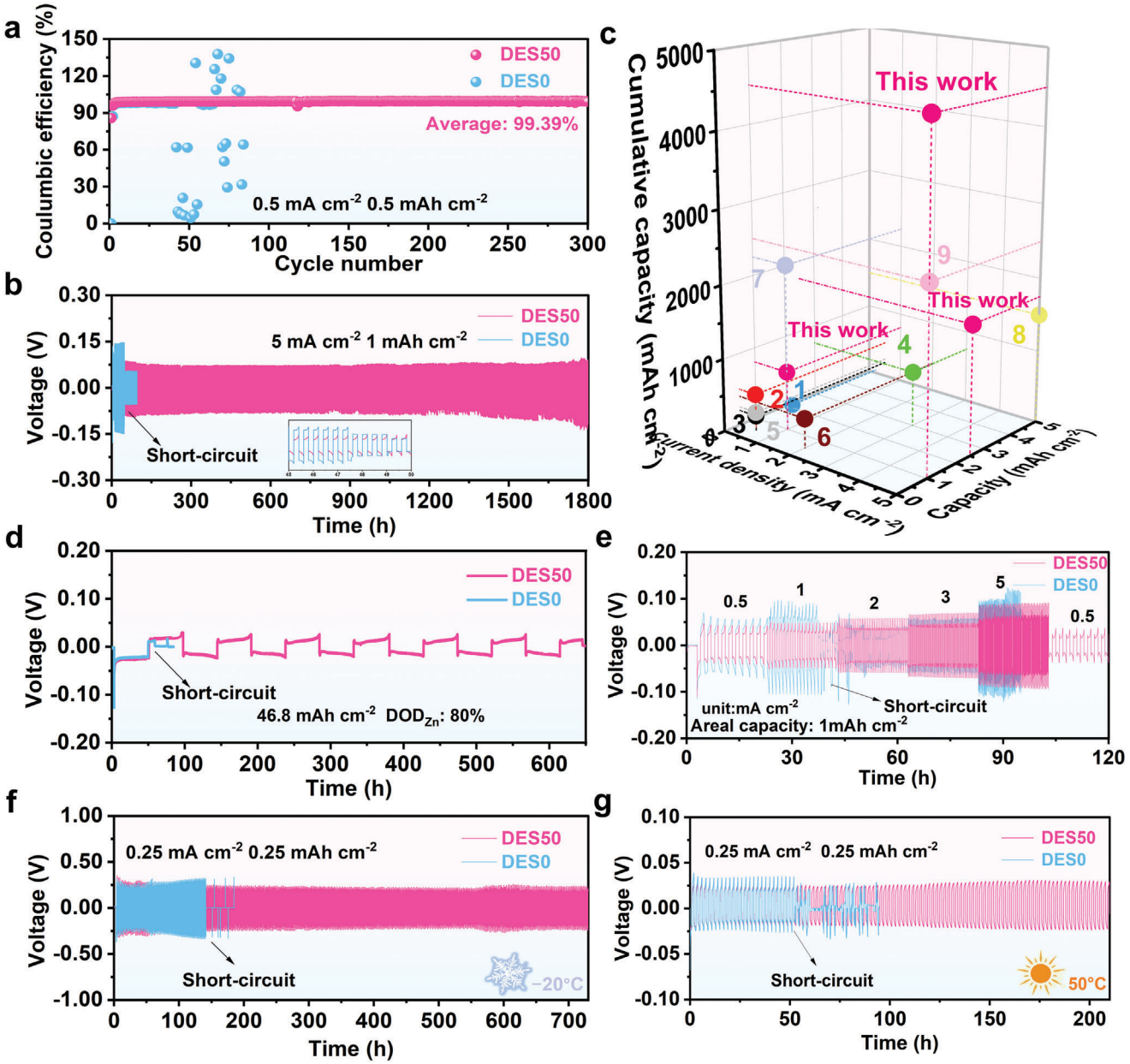

Figure 5. a) CEs of Zn//Cu cells in DES0 and DES50 at 0.5 mA cm^{-2} and 0.5 mAh cm^{-2}. b) Cycling performance of Zn//Zn symmetrical cells in DES0 and DES50 (5 mA cm^{-2} and 1 mAh cm^{-2}). c) The comparison of the DES50 system with recent reports focusing on eutectic electrolytes. d) Cycling performance of symmetric Zn cells at a zinc utilization rate (ZUR) of 80%. e) Rate performance of the Zn//Zn symmetric cells with a fixed plating capacity of 1 mAh cm^{-2}. Cycling performance of Zn//Zn symmetrical cells at f) −20 °C and g) 50 °C (0.25 mA cm^{-2} and 0.25 mAh cm^{-2}).

respectively. As shown in Figure 6b, the shape of the CV redox peak does not change after the addition of AEV, indicating that the DES50 electrolyte has little effect on the redox behavior of VOX cathode. Besides, the Zn//VOX full cell with DES50 shows superior redox reversibility with a narrower voltage gap between the redox peaks, which matches well with the charge-discharge plateaus in the voltage profiles, indicating higher electrochemical activity in the presence of AEV. The better electrochemical activity can be evidenced by the lower charge transfer impedance (~38.8 Ω) in the EIS spectrum results (Figure S28, Supporting Information). As a consequence, the Zn//VOX full cell in DES50 displays better rate performance than the cell in the DES0 electrolyte at all the current densities ranging from 0.1 to 5 A g^{-1}, and back to 0.1 A g^{-1}. Battery storage life is a crucial factor to evaluate battery performance, particularly for aqueous rechargeable energy storage systems. As displayed in Figure S29 (Supporting Information), after 24 h rest, the Zn//VOX cell using the DES50 electrolyte holds a higher capacity retention (90.3%) than that with the DES0 electrolyte (84.30%). The better storge performance would contribute to a longer cycling life of the battery. As expected, the cell working in the DES0 electrolyte shows the specific capacity fading from

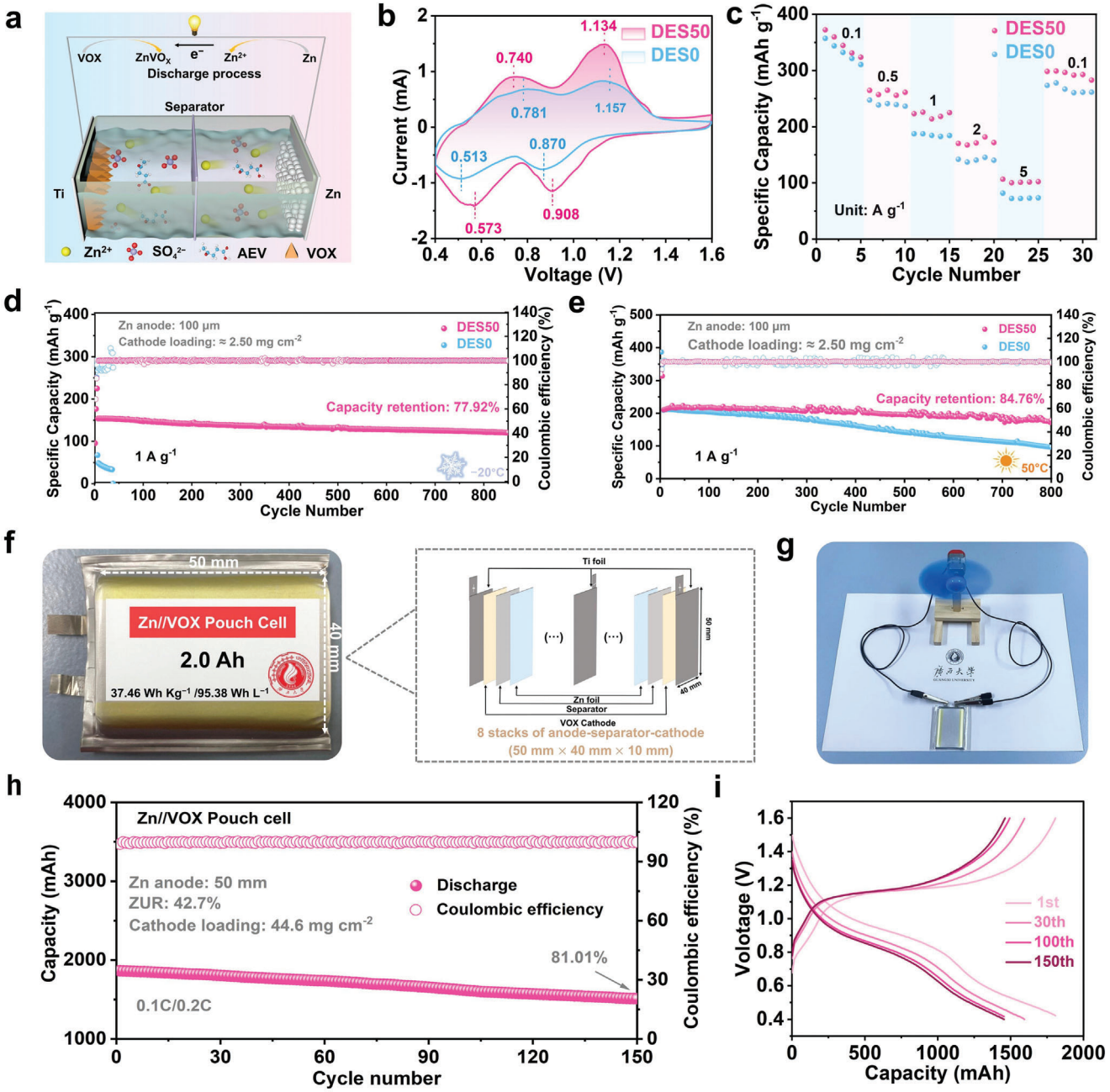

Figure 6. a) Schematic illustration of the discharge process in a Zn//VOX full battery with DES50 electrolyte. b) The CV curves of the Zn//VOX cells in DES0/DES50. c) Rate performance, and long-term cycling performance at 1 A g^{-1} at d) −20 °C and e) 50 °C, respectively. f) The photo of the designed 2.0-Ah Zn//VOX pouch cell and illustration of the internal configuration. g) The exhibition of the pouch cells powering a small fan. h) Cycling performance of the assembled pouch cell. i) Voltage-capacity curves at different cycles of the Zn//VOX pouch cell.

186.7 to 66.65 mAh g^{-1} after 1000 cycles, with a poor capacity reservation rate of 35.5%, which is mainly due to uncontrolled zinc dendrite growth and side reactions during cycling.[34] In sharp contrast, the battery in the DES50 electrolyte provides a superior capacity retention of 70.5% in the 1000th cycle, with the specific capacity maintained at 125.5 mAh g^{-1} (Figure S30, Supporting Information). Besides, the battery in the DES50 electrolyte of the long-term cycling performance at 0.1 A g^{-1} also displays an excellent capacity retention of 80.07% in the 100th cycle (Figure S31, Supporting Information). The significant improvement in the long-term cycle stability is mainly due to the addition of AEV co-solvents in the electrolyte, which promotes uniform Zn^{2+} deposition as well as inhibits the water-related side reactions, thus producing highly reversible Zn plating/striping performance upon cycling. Notably, the Zn//VOX cell using DES50 still delivers a capacity retention of 77.92% (850 cycles) and 84.76% (800 cycles) at the extreme temperatures of −20 and 50 °C, respectively (Figure 6d,e). The impressive coin

cell performance with DES50 eutectic electrolyte encourages us to package a large-capacity pouch cell to demonstrate the potential commercialization of the DES electrolyte. The pouch cell was fabricated by a bipolar structure with a size of 50 mm (length) × 40 mm (width) × 10 mm (thickness), which contains eight stacks of anode-separator-cathode (Figure 6f; Figure S32, Supporting Information). Based on the cell specifications (Table S2, Supporting Information), the Zn//VOX pouch cell capacity was designed to be 2.0 Ah, which, to the best of our knowledge, represents the large capacity family among the Ah-level AZMBs that has been seldomly reported.[42] The pouch cell is capable of driving the rotation of a small fan (Figure 6g). Under the practical conditions of double-side thick electrode (44.6 mg cm^{-2}), and thin Zn foil (50 µm) with a high ZUR of 42.7%, the pouch cell stably operates 150 cycles with a considerable retention of 81.01% of its initial capacity (Figure 6h,i). The actual energy density of the Zn//VOX pouch cell was calculated as high as 37.46 Wh Kg^{-1} and 95.38 Wh L^{-1} based on the whole pouch cell, which is almost twice of the popular all-vanadium flow battery,[43] demonstrating its high potential to be scaled up as safe and reliable energy storage devices.

3. Conclusion

In summary, we have designed a novel cost-effective eutectic electrolyte with triple functional regulation of water molecular behavior that utilizes small AEV molecules as the eutectic solvent to improve the overall performance of the AZMBs. First, in the DES50 eutectic electrolyte, the activity of free water is effectively reduced due to the strong interaction between AEV and H_2O that reshapes the hydrogen bonds network between water molecules. Second, the solvation structure of zinc ions is regulated with the decreased number of coordinated water. Lastly, the preferentially adsorbed AEV molecules impede the direct contact of the absorbed water at the Zn electrode interface. As a result, the symmetrical Zn cells cycle with DES50 electrolyte cycle for more than 1800 h (5 mA cm^{-2}, 1 mAh cm^{-2}) and 650 h even at a high DOD of 80%, which can also normally work even within a wide temperature range of −20–50 °C. Furthermore, the Zn//VOX full cells demonstrate excellent cycling stability and superior temperature tolerance. Most importantly, the packaged 2.0 Ah Zn//VOX pouch cell exhibits a high-capacity retention of 81.01% after 150 cycles, harvesting a remarkable actual energy density of 37.46 Wh Kg^{-1} and 95.38 Wh L^{-1} at the whole cell level. This work offers a significant reference to advance low-cost and high-performance aqueous zinc batteries from the perspective of triple regulation of water activity.

Supporting Information

Supporting Information is available from the Wiley Online Library or from the author.

Acknowledgements

This work was supported by the National Natural Science Foundation of China (22308066), the Natural Science Foundation of Guangxi Province (2024GXNSFAA010271), the Guangxi Science and Technology Base and Talent Special Project (Guike AD23026311), and the Opening Project of Guangxi Key Laboratory of Petrochemical Resource Processing and Process Intensification Technology (No. 2023K007). The authors also acknowledge the National High-Performance Computing Center Nanning Branch and Multifunctional Computer Center of Guangxi University for providing access to supercomputer resources. The authors would like to thank Jianliang Liao from Shiyanjia Lab (www.shiyanjia.com) for the XPS measurement.

Conflict of Interest

The authors declare no conflict of interest.

Data Availability Statement

The data that support the findings of this study are available from the corresponding author upon reasonable request.

Keywords

eutectic electrolyte, pouch cell, water activity, wide temperature, zinc ion batteries

Received: August 18, 2024
Revised: November 25, 2024
Published online: December 6, 2024

[1] a) X. L. Ji, *Energy Environ. Sci.* **2019**, *12*, 3203; b) S. Wu, Z. Hu, P. He, L. Ren, J. Huang, J. Luo, *eScience* **2023**, *3*, 100120; c) G. Wang, H. Fu, J. Lu, S. Huang, C. Pei, D. Min, Q. Zhang, H. S. Park, *Adv. Energy Mater.* **2024**, *14*, 2303549.
[2] H. He, H. Qin, J. Wu, X. Chen, R. Huang, F. Shen, Z. Wu, G. Chen, S. Yin, J. Liu, *Energy Storage Mater.* **2021**, *43*, 317.
[3] a) X. Yu, Z. Li, X. Wu, H. Zhang, Q. Zhao, H. Liang, H. Wang, D. Chao, F. Wang, Y. Qiao, H. Zhou, S. G. Sun, *Joule* **2023**, *7*, 1145; b) N. Hu, W. Lv, W. Chen, H. Tang, X. Zhang, H. Qin, D. Huang, J. Zhu, Z. Chen, J. Xu, H. He, *Adv. Funct. Mater.* **2023**, *34*, 2311773; c) P. Xiong, Y. Kang, N. Yao, X. Chen, H. Mao, W. S. Jang, D. M. Halat, Z. H. Fu, M. H. Jung, H. Y. Jeong, Y.-M. Kim, J. A. Reimer, Q. Zhang, H. S. Park, *ACS Energy Lett.* **2023**, *8*, 1613.
[4] a) C. Nie, G. Wang, D. Wang, M. Wang, X. Gao, Z. Bai, N. Wang, J. Yang, Z. Xing, S. Dou, *Adv. Energy Mater.* **2023**, *13*, 2300606; b) P. Xiong, C. Lin, Y. Wei, J. H. Kim, G. Jang, K. Dai, L. Zeng, S. Huang, S. J. Kwon, S. Y. Lee, H. S. Park, *ACS Energy Lett.* **2023**, *8*, 2718.
[5] X. Zeng, J. Mao, J. Hao, J. Liu, S. Liu, Z. Wang, Y. Wang, S. Zhang, T. Zheng, J. Liu, P. Rao, Z. Guo, *Adv. Mater.* **2021**, *33*, 2007416.
[6] X. Yun, Y. Chen, H. Gao, D. Lu, L. Zuo, P. Gao, G. Zhou, C. Zheng, P. Xiao, *Adv. Energy Mater.* **2024**, *14*, 2304341.
[7] C. Zhang, J. Holoubek, X. Wu, A. Daniyar, L. Zhu, C. Chen, D. P. Leonard, I. A. Rodríguez-Pérez, J. X. Jiang, C. Fang, X. Ji, *Chem. Commun.* **2018**, *54*, 14097.
[8] D. Han, T. Sun, R. Zhang, W. Zhang, T. Ma, H. Du, Q. Wang, D. He, S. Zheng, Z. Tao, *Adv. Funct. Mater.* **2022**, *32*, 2209065.
[9] X. Wang, Z. Zhang, B. Xi, W. Chen, Y. Jia, J. Feng, S. Xiong, *ACS Nano* **2021**, *15*, 9244.
[10] H. Liu, C. Zhao, X. Wu, C. Hu, F. Geng, M. Shen, B. Hu, B. Hu, C. Li, *Energy Environ. Sci.* **2024**, *17*, 668.
[11] a) J. Wu, Q. Liang, X. Yu, Q. F. Lü, L. Ma, X. Qin, G. Chen, B. Li, *Adv. Funct. Mater.* **2021**, *31*, 2011102; b) C. Zhang, L. Zhang, G. Yu, *Acc. Chem. Res.* **2020**, *53*, 1648; c) P. Jiang, L. Chen, H. Shao, S. Huang, Q. Wang, Y. Su, X. Yan, X. Liang, J. Zhang, J. Feng, Z. Liu, *ACS Energy Lett.* **2019**, *4*, 1419.

[12] W. Kao-Ian, R. Pornprasertsuk, P. Thamyongkit, T. Maiyalagan, S. Kheawhom, *J. Electrochem. Soc.* **2019**, *166*, A1063.
[13] X. Lin, G. Zhou, M. J. Robson, J. Yu, S. C. T. Kwok, F. Ciucci, *Adv. Funct. Mater.* **2022**, *32*, 2109322.
[14] J. Hao, L. Yuan, Y. Zhu, X. Bai, C. Ye, Y. Jiao, S. Z. Qiao, *Angew. Chem., Int. Ed.* **2023**, *62*, 202310284.
[15] J. Liu, C. Yang, X. Chi, B. Wen, W. Wang, Y. Liu, *Adv. Funct. Mater.* **2022**, *32*, 2106811.
[16] Y. Zhong, X. Xie, Z. Zeng, B. Lu, G. Chen, J. Zhou, *Angew. Chem., Int. Ed.* **2023**, *62*, 202310577.
[17] H. Hong, J. Zhu, Y. Wang, Z. Wei, X. Guo, S. Yang, R. Zhang, H. Cui, Q. Li, D. Zhang, C. Zhi, *Adv. Mater.* **2024**, *36*, 2308210.
[18] C. You, R. Wu, X. Yuan, L. Liu, J. Ye, L. Fu, P. Han, Y. Wu, *Energy Environ. Sci.* **2023**, *16*, 5096.
[19] Z. Li, Y. Liao, Y. Wang, J. Cong, H. Ji, Z. Huang, Y. Huang, *Energy Storage Mater.* **2023**, *56*, 174.
[20] B. Qiu, L. Xie, G. Zhang, K. Cheng, Z. Lin, W. Liu, C. He, P. Zhang, H. Mi, *Chem. Eng. J.* **2022**, *449*, 137843.
[21] a) G. Ma, L. Miao, Y. Dong, W. Yuan, X. Nie, S. Di, Y. Wang, L. Wang, N. Zhang, *Energy Storage Mater.* **2022**, *47*, 203; b) N. Hu, W. Lv, H. Tang, H. Qin, Y. Zhou, L. Yi, D. Huang, Z. Wu, J. Liu, Z. Chen, J. Xu, H. He, *J. Mater. Chem. A* **2023**, *11*, 14921.
[22] Q. Meng, R. Zhao, P. Cao, Q. Bai, J. Tang, G. Liu, X. Zhou, J. Yang, *Chem. Eng. J.* **2022**, *447*, 137471.
[23] M. M. Wu, X. C. Wang, F. Zhang, Q. Xiang, Y. Li, J. X. Guo, *Energy Environ. Sci.* **2023**, *16*, 5096.
[24] P. Sun, L. Ma, W. H. Zhou, M. J. Qiu, Z. L. Wang, D. L. Chao, W. J. Mai, *Angew. Chem., Int. Ed.* **2021**, *60*, 18247.
[25] M. Yan, K. Liu, Z. Jiang, *J. Electrochem. Soc.* **1996**, *408*, 225.
[26] S. Chen, D. Ji, Q. Chen, J. Ma, S. Hou, J. Zhang, *Nat. Commun.* **2023**, *14*, 3526.
[27] L. Hu, Y. Han, L. Yan, C. Zhu, Z. Xu, X. Zou, Y. Zhou, B. Xiang, *Energy Storage Mater.* **2024**, *65*, 103114.
[28] N. Hu, J. Tao, Y. Tan, H. Song, D. Huang, P. Liu, Z. Chen, X. Yin, J. Zhu, J. Xu, H. He, *Adv. Energy Mater.* **2024**, 2404018.
[29] H. Cao, X. Zhang, B. Xie, X. Huang, F. Xie, Y. Huo, Q. Zheng, R. Zhao, Q. Hu, L. Kang, S. Liu, D. Lin, *Adv. Funct. Mater.* **2023**, *33*, 2305683.
[30] H. Qin, W. Kuang, N. Hu, X. Zhong, D. Huang, F. Shen, Z. Wei, Y. Huang, J. Xu, H. He, *Adv. Funct. Mater.* **2022**, *32*, 226695.
[31] L. Liu, H. Lu, C. Han, X. Chen, S. Liu, J. Zhang, X. Chen, X. Wang, R. Wang, J. Xu, H. K. Liu, S. X. Dou, W. Li, *ACS Nano* **2023**, *17*, 23065.
[32] H. M. Badawi, W. Förner, B. El Ali, A. R. A. H. Al-Durais, *Spectrochim. Acta, Part A* **2008**, *70*, 983.
[33] Z. Cai, J. Wang, Y. Sun, *eScience* **2023**, *3*, 100093.
[34] H. Lu, X. Zhang, M. Luo, K. Cao, Y. Lu, B. B. Xu, H. Pan, K. Tao, Y. Jiang, *Adv. Funct. Mater.* **2021**, *31*, 2103514.
[35] X. Zhang, H. Weng, Y. Miu, W. Chen, N. Hu, W. Kuang, D. Huang, H. Du, J. Zhu, Z. Chen, J. Xu, H. He, *Chem. Eng. J.* **2024**, *482*, 148807.
[36] Z. M. Zhao, J. W. Zhao, Z. L. Hu, J. D. Li, J. J. Li, Y. J. Zhang, C. Wang, G. L. Cui, *Energy Environ. Sci.* **2019**, *12*, 1938.
[37] X. Xu, Y. Chen, D. Zheng, P. Ruan, Y. Cai, X. Dai, X. Niu, C. Pei, W. Shi, W. Liu, F. Wu, Z. Pan, H. Li, X. Cao, *Small* **2021**, *17*, 2101901.
[38] a) X. Liang, X. Chen, Z. Zhai, R. Huang, T. Yu, S. Yin, *Chem. Eng. J.* **2024**, *480*, 148040; b) K. Xie, K. Ren, Q. Wang, Y. Lin, F. Ma, C. Sun, Y. Li, X. Zhao, C. Lai, *eScience* **2023**, *3*, 100153.
[39] W. Chen, Y. Tan, C. Guo, X. Zhang, X. He, W. Kuang, H. Weng, H. Du, D. Huang, Y. Huang, J. Xu, H. He, *J. Colloid Interface Sci.* **2024**, *669*, 104.
[40] J. Wan, R. Wang, Z. Liu, S. Zhang, J. Hao, J. Mao, H. Li, D. Chao, L. Zhang, C. Zhang, *Adv. Mater.* **2023**, *36*, 2310623.
[41] H. Tang, N. Hu, L. Ma, H. Weng, D. Huang, J. Zhu, H. Yang, Z. Chen, X. Yin, J. Xu, H. He, *Adv. Funct. Mater.* **2024**, *34*, 2402484.
[42] a) A. Zhou, J. Zhang, M. Chen, J. Yue, T. Lv, B. Liu, X. Zhu, K. Qin, G. Feng, L. Suo, *Adv. Mater.* **2022**, *34*, 2207040; b) G. Liang, Z. Tang, B. Han, J. Zhu, A. Chen, Q. Li, Z. Chen, Z. Huang, X. Li, Q. Yang, C. Zhi, *Adv. Mater.* **2023**, *35*, 2210051; c) H. Yuan, J. Luan, J. Liu, N. Zhao, C. Zhong, *Chem. Eng. J.* **2023**, *457*, 141193.
[43] C. Zhang, Z. Yuan, X. Li, *ACS Energy Lett.* **2024**, *9*, 3456.